

On Obtaining High-Order Finite-Volume Solutions to the Euler Equations on Unstructured Meshes

Carl Ollivier-Gooch*, Amir Nejat† and Krzysztof Michalak‡
Advanced Numerical Simulation Laboratory
University of British Columbia

High-order finite volume schemes for unstructured meshes first appeared in the literature at least as early as Barth and Frederickson’s 1990 paper.¹ However, the approach has not gained a wide following, perhaps because of the difficulties in achieving a genuinely high-order accurate solution, especially when dealing with curved boundaries. In this paper, we document in detail our approach to constructing a high-order solver. In addition to reconstruction, we discuss flux integration and curved boundary treatment. We describe how we tackle each of these issues, provide useful testing procedures to verify code correctness, and illustrate the results of mis-handling various small but important details.

I. Introduction

Since Barth and Frederickson’s pioneering work,¹ a number of researchers have studied high-order (by which we mean third- and fourth-order accurate) finite-volume methods for computational aerodynamics using unstructured meshes^{2–9} For the most part, however, these researchers tend to content themselves primarily with showing that high-order schemes are superior in accuracy to second-order schemes without quantifying the order of accuracy of their scheme. Some of the research described in the literature also explicitly fails to implement all terms to high-order accuracy. These observation applies also to much of the research on high-order methods for computational aerodynamics on structured meshes [10–12, for instance]. Despite the accuracy benefits of high-order schemes on a particular mesh (which, it is fair to say, are relatively undisputed), these methods have not developed a wide following in the research community. We speculate that there are two reasons for this: first, developing a genuinely high-order accurate flow solver requires attention to a large number of details, many of which are not documented in the literature; and second, high-order schemes are perceived as requiring prohibitive CPU time and/or memory. This paper will address the first of these issues by relating our experience^{4, 13–18} in developing and demonstrating a high-order accurate solver for the Euler equations. The issue of efficiency, on which we have also made significant progress, is the topic of a companion paper. *Cite the Miami efficiency paper, once there’s something to cite.*

This paper is intended as and organized to be a practical guide in the construction of a high-order accurate finite-volume flow solver. We discuss in turn important, if sometimes subtle, issues related to solution reconstruction (Section II), flux integration (Section III), and curved boundary treatment (Section IV). In each section, we describe a key element for achieving high-order accuracy as well as the testing procedures we have developed in verifying our code and the descriptions of common pitfalls in algorithm development, including examples of the effects of these potential errors. Finally, Section V contains a summary and some concluding remarks.

II. Solution Reconstruction

The first and most obvious feature of a high-order accurate unstructured mesh finite-volume solver is a high-order reconstruction. Although there are other alternatives for second-order schemes (notably Green-Gauss reconstruction), obtaining higher than second-order accuracy requires an explicit polynomial reconstruction. In this work, we will focus on k -exact least-squares reconstruction (see,^{2, 5, 14} for instance); the use of ENO³ or WENO^{7, 8} reconstruction would

*Associate Professor, Member AIAA. cfog@mech.ubc.ca

†PhD student, Student member AIAA. nejat@mech.ubc.ca

‡PhD student, Student member AIAA. michalak@mech.ubc.ca

alter the approach taken to compute reconstruction polynomials, though not the need to properly ensure conservation of the mean, as described below.

The techniques of high-order accurate k -exact reconstruction are well documented elsewhere, and here we will content ourselves with a brief summary, referring interested readers to Barth and Frederickson¹ or Ollivier-Gooch and Van Altena¹⁴ for details.

In the finite-volume method, the domain is tessellated into non-overlapping control volumes. Each control volume V_i has a geometric reference point \bar{x}_i . While in principle any point can be chosen as the reference point, the usual choices (which we recommend) are the cell centroid for cell-centered control volumes and the vertex for vertex-centered control volumes. For any smooth function $u(\bar{x})$ and its control-volume averaged values \bar{u}_i , the k -exact least-squares reconstruction will use a compact stencil in the neighborhood of control volume i to compute an expansion $R_i(\bar{x} - \bar{x}_i)$ that conserves the mean in control volume i and reconstructs exactly polynomials of degree $\leq k$ (equivalently, $R_i(\bar{x} - \bar{x}_i) - u(\bar{x}) = O(\Delta x^{k+1})$).

Conservation of the mean requires that the average of the reconstructed function R_i and the original function u over control volume i be the same:

$$\frac{1}{V_i} \int_{V_i} R_i(\bar{x} - \bar{x}_i) dA = \frac{1}{V_i} \int_{V_i} u(\bar{x}) dA \equiv \bar{u}_i. \quad (1)$$

The expansion $R_i(\bar{x} - \bar{x}_i)$ can be written as:

$$\begin{aligned} R_i(\bar{x} - \bar{x}_i) &= u|_{\bar{x}_i} + \frac{\partial u}{\partial x} \Big|_{\bar{x}_i} (x - x_i) + \frac{\partial u}{\partial y} \Big|_{\bar{x}_i} (y - y_i) \\ &\quad + \frac{\partial^2 u}{\partial x^2} \Big|_{\bar{x}_i} \frac{(x - x_i)^2}{2} + \frac{\partial^2 u}{\partial x \partial y} \Big|_{\bar{x}_i} ((x - x_i)(y - y_i)) + \frac{\partial^2 u}{\partial y^2} \Big|_{\bar{x}_i} \frac{(y - y_i)^2}{2} + \dots \end{aligned} \quad (2)$$

Taking the control volume average of this expansion over control volume i and equating it to the mean value gives

$$\bar{u}_i = u|_{\bar{x}_i} + q|_{\bar{x}_i} \bar{x}_i + \frac{\partial u}{\partial y} \Big|_{\bar{x}_i} \bar{y}_i + \frac{\partial^2 u}{\partial x^2} \Big|_{\bar{x}_i} \frac{\bar{x}^2}{2} + \frac{\partial^2 u}{\partial x \partial y} \Big|_{\bar{x}_i} \bar{x} \bar{y} + \frac{\partial^2 u}{\partial y^2} \Big|_{\bar{x}_i} \frac{\bar{y}^2}{2} + \dots \quad (3)$$

where

$$\overline{x^n y^m}_i \equiv \frac{1}{A_i} \int_{V_i} (x - x_i)^n (y - y_i)^m dA. \quad (4)$$

are control volume moments.

k th-order accuracy requires that we compute the k th derivatives by minimizing the error in predicting the mean value of the reconstructed function for control volumes in the stencil $\{V_j\}_i$; that is, by minimizing the difference between the actual control volume average \bar{u}_j and the average of R_i over control volume j . The mean value, for a single control volume V_j , of the reconstructed function R_i is

$$\begin{aligned} \frac{1}{A_j} \int_{V_j} R_i(\bar{x} - \bar{x}_i) dA &= u|_{\bar{x}_i} + \frac{\partial u}{\partial x} \Big|_{\bar{x}_i} \left(\frac{1}{A_j} \int_{V_j} (x - x_i) dA \right) + \frac{\partial u}{\partial y} \Big|_{\bar{x}_i} \left(\frac{1}{A_j} \int_{V_j} (y - y_i) dA \right) \\ &\quad + \frac{\partial^2 u}{\partial x^2} \Big|_{\bar{x}_i} \left(\frac{1}{2A_j} \int_{V_j} (x - x_i)^2 dA \right) + \frac{\partial^2 u}{\partial x \partial y} \Big|_{\bar{x}_i} \left(\frac{1}{A_j} \int_{V_j} (x - x_i)(y - y_i) dA \right) \\ &\quad + \frac{\partial^2 u}{\partial y^2} \Big|_{\bar{x}_i} \left(\frac{1}{2A_j} \int_{V_j} (y - y_i)^2 dA \right) + \dots \end{aligned} \quad (5)$$

To avoid computing moments of each control volume in $\{V_j\}_i$ about \bar{x}_i , replace $x - x_i$ and $y - y_i$ with $(x - x_j) + (x_j - x_i)$ and $(y - y_j) + (y_j - y_i)$, respectively. Expanding and integrating, we obtain

$$\begin{aligned} \frac{1}{A_j} \int_{V_j} R_i(\bar{x} - \bar{x}_i) &= u|_{\bar{x}_i} + \frac{\partial u}{\partial x} \Big|_{\bar{x}_i} (\bar{x}_j + (x_j - x_i)) + \frac{\partial u}{\partial y} \Big|_{\bar{x}_i} (\bar{y}_j + (y_j - y_i)) \\ &\quad + \frac{\partial^2 u}{\partial x^2} \Big|_{\bar{x}_i} \frac{\bar{x}_j^2 + 2\bar{x}_j(x_j - x_i) + (x_j - x_i)^2}{2} \\ &\quad + \frac{\partial^2 u}{\partial x \partial y} \Big|_{\bar{x}_i} (\bar{x} \bar{y}_j + \bar{x}_j(y_j - y_i) + (x_j - x_i)\bar{y}_j + (x_j - x_i)(y_j - y_i)) \\ &\quad + \frac{\partial^2 u}{\partial y^2} \Big|_{\bar{x}_i} \frac{\bar{y}_j^2 + 2\bar{y}_j(y_j - y_i) + (y_j - y_i)^2}{2} + \dots \end{aligned} \quad (6)$$

This equation is written for every control volume in the stencil (of which there must be more than the number of derivatives to be computed). Together with the mean constraint, these error equations and the mean constraint form a constrained least-squares system:

$$\begin{bmatrix} 1 & \bar{x} & \bar{y} & \bar{x}^2 & \bar{x}\bar{y} & \bar{y}^2 & \cdots \\ w_{i1} & w_{i1}\widehat{x}_{i1} & w_{i1}\widehat{y}_{i1} & w_{i1}\widehat{x}_{i1}^2 & w_{i1}\widehat{x}_{i1}\widehat{y}_{i1} & w_{i1}\widehat{y}_{i1}^2 & \cdots \\ w_{i2} & w_{i2}\widehat{x}_{i2} & w_{i2}\widehat{y}_{i2} & w_{i2}\widehat{x}_{i2}^2 & w_{i2}\widehat{x}_{i2}\widehat{y}_{i2} & w_{i2}\widehat{y}_{i2}^2 & \cdots \\ w_{i3} & w_{i3}\widehat{x}_{i3} & w_{i3}\widehat{y}_{i3} & w_{i3}\widehat{x}_{i3}^2 & w_{i3}\widehat{x}_{i3}\widehat{y}_{i3} & w_{i3}\widehat{y}_{i3}^2 & \cdots \\ \vdots & \vdots & \vdots & \vdots & \vdots & \vdots & \ddots \\ w_{iN} & w_{iN}\widehat{x}_{iN} & w_{iN}\widehat{y}_{iN} & w_{iN}\widehat{x}_{iN}^2 & w_{iN}\widehat{x}_{iN}\widehat{y}_{iN} & w_{iN}\widehat{y}_{iN}^2 & \cdots \end{bmatrix} \begin{pmatrix} u \\ \frac{\partial u}{\partial x} \\ \frac{\partial u}{\partial y} \\ \frac{1}{2}\frac{\partial^2 u}{\partial x^2} \\ \frac{\partial^2 u}{\partial x\partial y} \\ \frac{1}{2}\frac{\partial^2 u}{\partial y^2} \\ \vdots \end{pmatrix}_i = \begin{pmatrix} \bar{u}_i \\ \bar{u}_1 \\ \bar{u}_2 \\ \bar{u}_3 \\ \vdots \\ \bar{u}_N \end{pmatrix}, \quad (7)$$

where the first row is the mean constraint, and the geometric terms have been abbreviated as

$$\begin{aligned} \widehat{x^n y^m}_{ij} &\equiv \frac{1}{A_j} \int_{V_j} ((x-x_j) + (x_j-x_i))^n ((y-y_j) + (y_j-y_i))^m dA \\ &= \sum_{l=0}^m \left\{ \frac{m!}{l!(m-l)!} (y_j-y_i)^l \sum_{k=0}^n \left[\frac{n!}{k!(n-k)!} (x_j-x_i)^k \overline{x^{n-k} y^{m-l}}_j \right] \right\} \end{aligned} \quad (8)$$

and the weights are set to emphasize geometrically nearby data:

$$w_{ij} = \frac{1}{|\bar{x}_j - \bar{x}_i|^p}. \quad (9)$$

Note that there is some question about the optimal choice of the exponent p used in this weight; we find that for inviscid problems choosing $p = 1$ is typically the best choice in terms of promoting rapid convergence.^a

As a practical matter, the control volume moments defined by Equation 4 are easiest to compute by using Gauss's theorem to convert them to integrals around V_i .

$$\overline{x^n y^m} = \frac{1}{(n+1)A_i} \int_{\partial V_i} (x-x_i)^{n+1} (y-y_i)^m \hat{n}_x ds \quad (10)$$

where \hat{n}_x is the x -component of the outward unit normal on the control volume boundary, and similarly in three dimensions. Converting the integral to a contour integral by using Green's theorem gives identical 2D results in theory. In practice, for straight control volume boundaries, the numerical integration is identical as well; however, for curved control volume boundaries (see Section IV), Gauss's theorem gives an integral that is much easier to evaluate numerically. The integrals of Equation 10 may be evaluated exactly by using a Gaussian quadrature of appropriate order along each segment of the boundary of the control volume, as described in Table 1. Moment calculations can be verified by hand for individual control volumes. A less laborious check that is also effective is to use the generalization of the parallel axis theorem to compute moments for the entire domain by combining the moments of individual control volumes. That is, one can compute

$$\begin{aligned} \int_{\Omega} x^n y^m dA &= \sum_{\text{CV}} \int_{\text{CV}} x^n y^m dA \\ &= \sum_{\text{CV}} \int_{\text{CV}} (x-x_i+x_i)^n (y-y_i+y_i)^m dA \end{aligned}$$

The latter integral is exactly equivalent to computing $\widehat{x^n y^m}_{ij}$, of Equation 8, with $\bar{x}_i = 0$. While this test is not completely rigorous, passing this test for all moments with broken moment calculation code would require such an unlikely chain of coincidences that we have confidence in the test.

Typically, the least-squares problem of Equation 7 is actually coded with the mean constraint eliminated analytically. After solving the remaining unconstrained least-squares problem, the mean constraint (Equation 1) must be used to compute the constant term in the expansion.

^aFor viscous flows, the situation is even less clear. Several researchers have studied this topic for second-order schemes.^{19,20}

Moment	Required for Order \geq	Number of Gauss Points
Area	1	1
\bar{x}, \bar{y}	2	2
$\bar{x}^2, \bar{xy}, \bar{y}^2$	3	2
$\bar{x}^3, \bar{x}^2\bar{y}, \bar{xy}^2, \bar{y}^3$	4	3

Table 1. The minimum number of quadrature points required for computing control volume moments by integration around the control volume, *a la* Equation 10.

The correctness of reconstruction can be tested by confirming that all monomials of degree $\leq k$ are reconstructed exactly. A prerequisite for this test, obviously, is that control volume averages can be computed to at least the order of accuracy of the reconstruction being tested; see Section IV for details on how to do this for control volumes with curved boundaries. We recommend using this test, as it is both a complete test and an efficient one, in that errors in correctly reconstructing a particular monomial are nearly always traceable to errors in the corresponding column of the least-squares system, either in moment calculation or matrix assembly.

In addition to testing monomials, we also recommend testing reconstruction of an arbitrary smooth function on a geometrically simple domain, to confirm that both maximum error (L_∞ norm) and average error (L_1 and/or L_2 norms) behave as expected. We show here the results of reconstructing the function

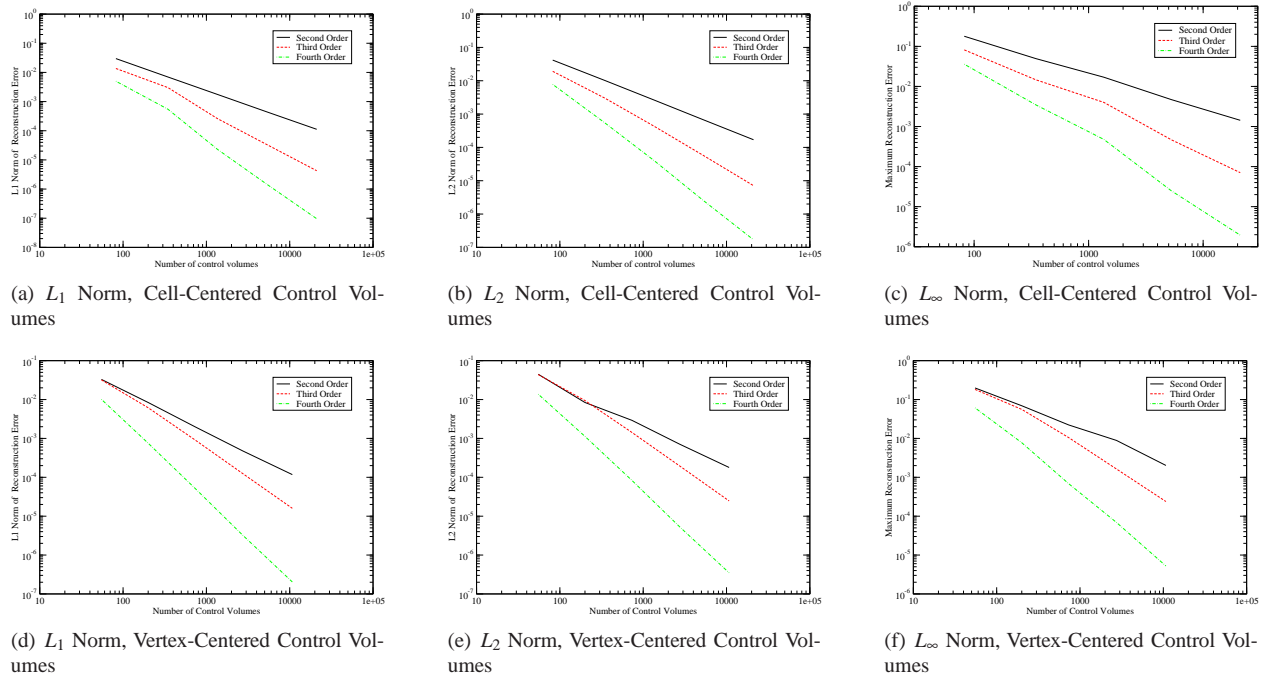
$$f(x, y) = \sin(\pi x) \cos(2\pi y)$$

over the square domain $[0, 1] \times [0, 1]$. A series of five quasi-uniform triangular meshes was generated within a unit square, ranging in size from 82 to 21087 cells (55 to 10746 vertices). The test function $f(x, y)$ was averaged over the control volumes using a six-order accurate quadrature rule,²¹ and these control volume averages were reconstructed using linear, quadratic, and cubic reconstruction. Reconstruction error is assessed in the L_1 and L_2 norms by integrating the difference between original function and the reconstruction over the domain, control volume by control volume, again using a sixth-order quadrature to avoid muddying the waters with integration errors. The L_∞ norm is evaluated by finding the largest difference between the function and reconstruction at any of the quadrature points in the domain. The results are shown in Figure 1. As expected, both cell- and vertex-centered schemes show well-behaved convergence of the reconstruction to the original function, in the sense that asymptotic convergence rates are achieved even for very coarse meshes. In addition, the reconstruction error is always decreased by increasing the order of accuracy for cell-centered schemes; for vertex-centered reconstruction on very coarse meshes, this case shows little difference between the linear and quadratic reconstructions. Finally, the accompanying table shows the computed asymptotic order of accuracy, based on the three finest meshes; in all cases, the nominal order is achieved for the L_1 and L_2 norms; the data for L_∞ norms, while less perfectly behaved, still shows convergence rates that are quite close to the nominal order of accuracy, especially for cell-centered control volumes.

Equation 3 clearly implies that the value at the control volume reference point must be computed explicitly rather than simply using the control volume average as the reference point value u_i in the expansion of R_i . Neglecting this key point introduces a second-order error in the solution reconstruction when the control volume centroid is used at the reference point, as shown in Figure 2a for the L_2 norm. The high-order schemes degenerate to second-order accuracy in this case, with somewhat less error than the second-order scheme because curvature effects are captured by the reconstruction; also, note that the broken third- and fourth-order schemes show identical behavior for fine meshes, where the differences between them are swamped by the large error in the mean value. For vertex-centered control volumes, the situation is even worse, with even a linear reconstruction producing errors if the offset is not taken into account, as shown in Figure 2b, with the largest errors in practice falling near the domain boundary, where the distance between vertices and control volume centroids is the largest.

III. Flux Integration

Given a correct high-order reconstruction, as described in the previous section, correct high-order flux calculation is a straightforward matter of applying a flux function. To compute a high-order flux integral from this high-order flux data requires a numerical quadrature scheme of commensurate accuracy. In two dimensions, we prefer Gauss quadrature because of its efficiency: Gauss quadrature with n points can exactly integrate polynomials of degree $2n - 1$. For flux integration in three dimensions, quadrature rules are more complex; we integrate over triangles using the following rules recommended by Stroud and Secrest:²¹



Control Volume Type	Nominal Order	Actual Asymptotic Order		
		L_1	L_2	L_∞
Cell	2	2.008	1.996	1.805
	3	3.000	2.990	2.944
	4	3.994	3.983	3.996
Vertex	2	2.107	2.079	1.786
	3	3.013	3.021	2.819
	4	4.123	4.075	3.628

Figure 1. Errors in a correct reconstruction scheme will converge at the nominal order of accuracy in all norms.

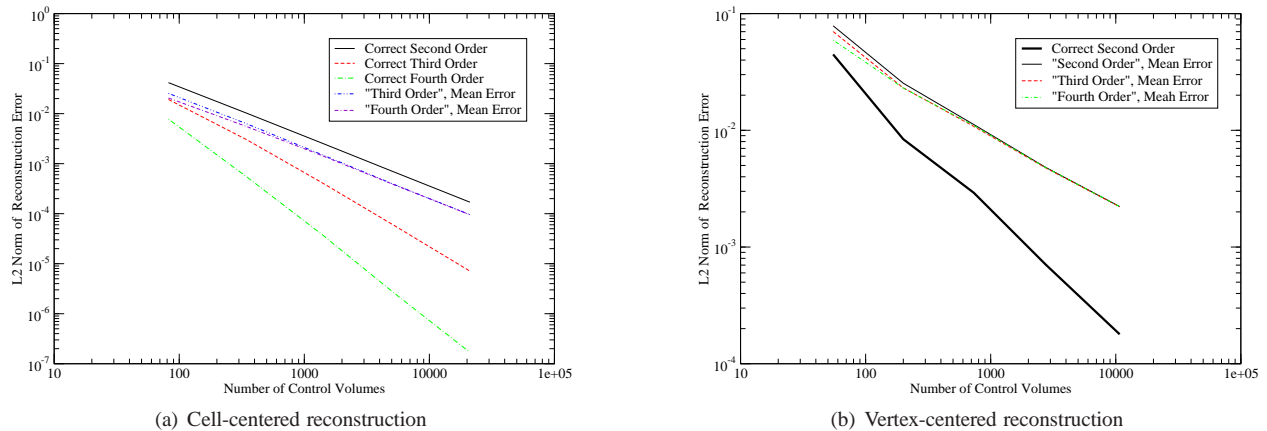


Figure 2. The effects of failing to properly conserve the mean in computing a high-order reconstruction are severe, reducing all schemes to second-order accuracy for cell-centered control volumes, and to first-order accuracy for vertex-centered control volumes.

	Point Location	Weight
Second-order (centroid)	$(\frac{1}{3}, \frac{1}{3}, \frac{1}{3})$	1
Third-order (edge mid-sides)	$(\frac{1}{2}, \frac{1}{2}, 0)$	$\frac{1}{3}$
	$(\frac{1}{2}, 0, \frac{1}{2})$	$\frac{1}{3}$
	$(0, \frac{1}{2}, \frac{1}{2})$	$\frac{1}{3}$
Fourth-order (centroid plus three interior points)	$(\frac{1}{3}, \frac{1}{3}, \frac{1}{3})$	$-\frac{9}{16}$
	$(\frac{1}{5}, \frac{1}{5}, \frac{3}{5})$	$\frac{25}{48}$
	$(\frac{1}{5}, \frac{3}{5}, \frac{1}{5})$	$\frac{25}{48}$
	$(\frac{3}{5}, \frac{1}{5}, \frac{1}{5})$	$\frac{25}{48}$

Table 2. Quadrature points and weights for triangles, which we apply for flux integration in three dimensions and for source term integration in two dimensions. All point locations are given in barycentric coordinates, and weights are normalized by triangle area. Note that the negative weight for the centroid in this last quadrature rule could conceivably cause problems, especially for rapidly varying flux functions. However, we have been unable to find a quadrature rule with positive coefficients *and* all quadrature points on or inside the triangle.

Once flux integration code has been written, we recommend testing it by comparing the computed flux integral with the integral over the control volume of the flux divergence. That is, we recommend demonstrating that

$$\int_{CV} \nabla \cdot \vec{F} dV = \oint_{\partial CV} \vec{F} \cdot \hat{n} dA$$

in the discrete version to within truncation error, as Gauss's theorem requires. This test requires specifying a physically plausible analytic solution (for instance, density and pressure must be positive), along with coding the divergence of the flux for this solution explicitly. This approach is a simplified variant on the Method of Manufactured Solutions,²² in which only the flux integral is verified, rather than the entire code. In particular, we typically choose to ignore boundary condition issues, leaving verification of boundary conditions for a separate step.

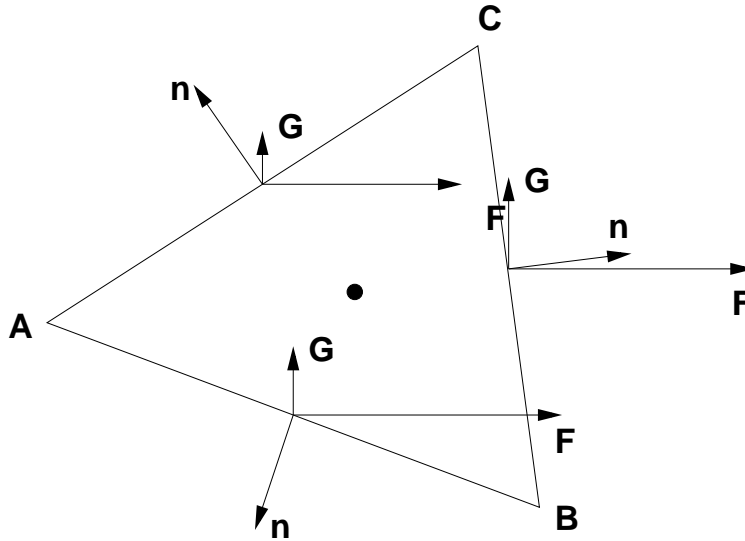


Figure 3. Control volume used in analysis of the order of accuracy of flux integration, including fluxes and surface normals.

Before examining results, however, we should determine what order of accuracy we expect to see in the computed flux integrals. Consider the triangular control volume illustrated in Figure 3, and a second-order accurate scheme (which implies a single Gauss point at the mid-side of each edge of the triangle). Now, the flux integral around this triangle can be written as

$$\oint_{ABC} \mathcal{F} \cdot \hat{n} ds = \sum \mathcal{F}_i \cdot \hat{n}_i l_i$$

where the sum is taken over all segments in the control volume boundary, $\mathcal{F} \equiv F\hat{i} + G\hat{j}$, \mathcal{F}_i is evaluated at the mid-side of the i th face of the control volume, and l_i is the length of that face. The fluxes F and G can be expanded in a Taylor series about the control volume reference point \vec{x}_0 :

$$\begin{aligned} F_i &= F_0 + \frac{\partial F}{\partial x} \Delta x_i + \frac{\partial F}{\partial y} \Delta y_i + \frac{\partial^2 F}{\partial x^2} \frac{\Delta x_i^2}{2} + \frac{\partial^2 F}{\partial x \partial y} \Delta x_i \Delta y_i + \frac{\partial^2 F}{\partial y^2} \frac{\Delta y_i^2}{2} + \dots \\ G_i &= G_0 + \frac{\partial G}{\partial x} \Delta x_i + \frac{\partial G}{\partial y} \Delta y_i + \frac{\partial^2 G}{\partial x^2} \frac{\Delta x_i^2}{2} + \frac{\partial^2 G}{\partial x \partial y} \Delta x_i \Delta y_i + \frac{\partial^2 G}{\partial y^2} \frac{\Delta y_i^2}{2} + \dots \end{aligned}$$

Inserting these in the sum and regrouping, we get:

$$\begin{aligned} \sum \mathcal{F}_i \cdot \hat{n}_i l_i &= F_0 (\sum n_{x,i} l_i) + G_0 (\sum n_{y,i} l_i) \\ &+ \sum \left(\frac{\partial F}{\partial x} \Delta x_i + \frac{\partial F}{\partial y} \Delta y_i \right) n_{x,i} l_i + \sum \left(\frac{\partial G}{\partial x} \Delta x_i + \frac{\partial G}{\partial y} \Delta y_i \right) n_{y,i} l_i \\ &+ \sum \left(\frac{\partial^2 F}{\partial x^2} \frac{\Delta x_i^2}{2} + \frac{\partial^2 F}{\partial x \partial y} \Delta x_i \Delta y_i + \frac{\partial^2 F}{\partial y^2} \frac{\Delta y_i^2}{2} \right) n_{x,i} l_i \\ &+ \sum \left(\frac{\partial^2 G}{\partial x^2} \frac{\Delta x_i^2}{2} + \frac{\partial^2 G}{\partial x \partial y} \Delta x_i \Delta y_i + \frac{\partial^2 G}{\partial y^2} \frac{\Delta y_i^2}{2} \right) n_{y,i} l_i + \dots \end{aligned} \quad (11)$$

The first line in Equation 11 is identically zero for a closed control volume. The second line is the result we actually want to compute: the integral of the flux divergence over the control volume; note that it is a second-order quantity in the characteristic length for the cell, as Δx , Δy , and l_i are all proportional to edge length. The third and fourth lines are third-order terms in the characteristic length, and these are terms which are not correct in the second-order scheme. More precisely, the second derivative terms are explicitly missing from the solution reconstruction, which implies that any evaluation of the fluxes based on the (linear) reconstruction will not have a sufficiently accurate solution to compute the second derivative terms in the expansion of the fluxes.^b Because we choose are comparing $\sum \mathcal{F}_i \cdot \hat{n}_i l_i$ to the analytic flux divergence $\int \nabla \cdot \mathcal{F} dA$, we expect to measure a third-order error in flux integration with a second-order accurate reconstruction. For higher orders of accuracy, we can conclude from analogous arguments that we again expect flux integration error to be one order smaller than the reconstruction error. Also, although the accompanying sketch showed a cell-centered control volume, the same argument, and even the same mathematics, applies to vertex-centered control volumes.

Though the results of this analysis are perhaps counter-intuitive, the analysis is consistent with the observed behavior of real solvers, which are capable of producing a k -order accurate approximation to the exact solution of a problem from a k -order accurate reconstruction. One way to confirm this is by considering the effect, for a second-order scheme, of a second-order perturbation to the solution. Such a perturbation produces a second-order change in the mean fluxes F_0 and G_0 , but a first-order perturbation in the gradients of the fluxes ($\frac{\partial F}{\partial x}$, etc), because flux gradients depend directly on solution gradients, which in turn are only computed to first-order accuracy. This will cause a first-order change in the terms in line 2 of Equation 11 (before multiplication by Δx_i and l_i), which is the correct magnitude to cancel the errors in higher flux derivatives. Thus, at least on an order of magnitude basis, we can reasonably expect that solutions that differ by only $O(h^k)$ can produce flux integrals that differ by $O(h^{k+1})$ in the measure we use.

For our present purposes in testing the flux integral for the Euler equations in two dimensions, we specify an arbitrary solution in primitive variables

$$\begin{aligned} \rho &= 1 + \rho_0 \sin(\pi x) \sin(\pi y) \\ u &= u_0 \sin(\pi x) \cos(2\pi y) \\ v &= v_0 \cos(2\pi x) \sin(\pi y) \\ P &= \frac{1}{\gamma} + P_0 \sin(2\pi x) \sin(2\pi y) \end{aligned}$$

We use the same sequence of meshes as in the reconstruction test. Roe's flux function was used in the interior, but the results are not sensitive to the choice of flux function, because the solution is smooth. No physical boundary condition was applied; instead, the analytic flux was computed at the boundary based on reconstructed data. All the perturbation

^bIt is worth noting here that structured mesh schemes achieve a one-order better flux integral because of cancellation in the error terms, at least for even orders of accuracy.

magnitudes — ρ_0 , u_0 , v_0 , and P_0 — were set to 0.1. We present results in Figure 4 for the L_2 norms of the error in the energy flux integral; the energy flux integral produces the largest magnitude of error for this case, and the behavior of the L_2 norm is representative of the other cases. This flux integral data clearly meets the expected accuracy level of $O(h^{k+1})$

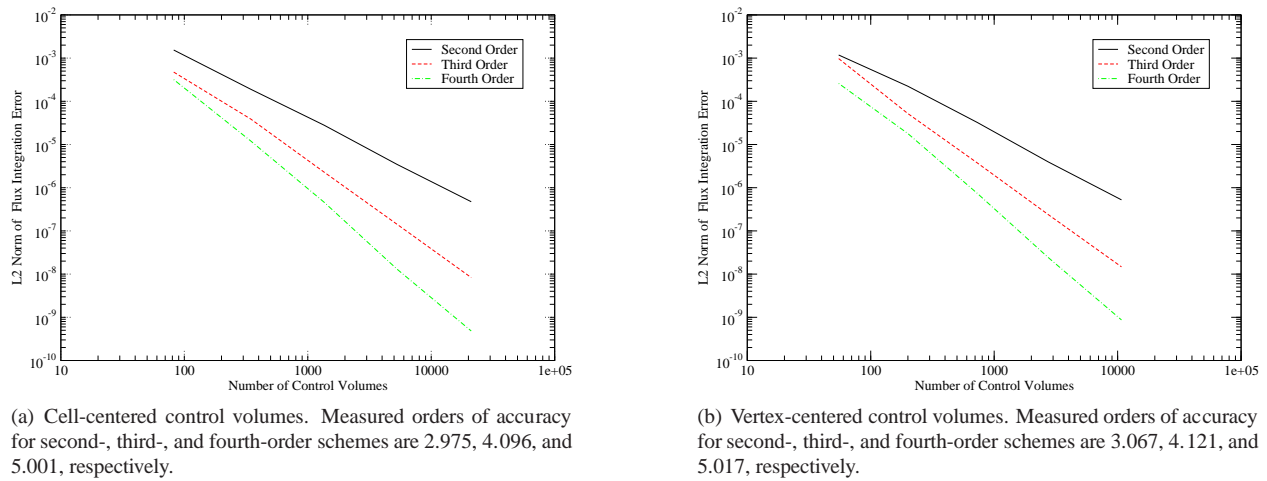


Figure 4. Errors in a correct flux integral for the Euler equations converge one order slower than the reconstruction.

The importance of having the correct number of Gauss points for high-order schemes can be seen in Figure 5. Essentially, the high-order schemes are behaving like expensive second-order schemes, with little difference in the flux integrals. This result is expected, in that the single-point Gauss quadrature is known to be only second-order accurate.

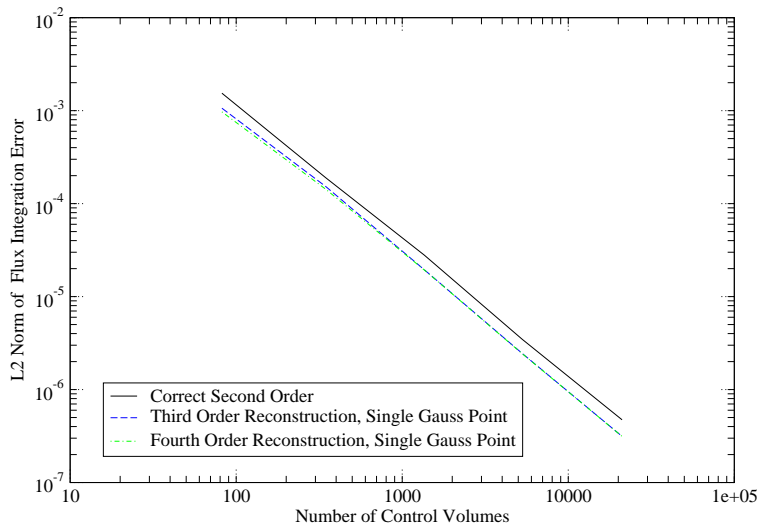


Figure 5. Using the correct number of Gauss points when computing high-order flux integrals is essential; using only a single Gauss point reduces accuracy to second order.

A. Source Term Integration

For many problems, accurate calculation of source terms is also required; we include a description here for completeness, even though these quadrature rules are unnecessary for the Euler equations. For second-order schemes, it is sufficient to use a single quadrature point located at the control volume centroid. For third- and fourth-order accurate schemes, more quadrature points are required. In two dimensions, the quadrature rules described in the previous section can be applied directly for cell-centered control volumes, while vertex-centered control volumes must be de-

composed into triangles before they can be integrated. In three dimensions, multi-point quadrature rules for tetrahedra must be used; again, quadrature point locations are given in barycentric coordinates.

Second order (centroid):

Point location	Weight
$(\frac{1}{4}, \frac{1}{4}, \frac{1}{4}, \frac{1}{4})$	1

Third order (four interior points):

Point location	Weight
(r, r, r, s)	$\frac{1}{4}$
(r, r, s, r)	$\frac{1}{4}$
(r, s, r, r)	$\frac{1}{4}$
(s, r, r, r)	$\frac{1}{4}$

$$\text{where } r = \frac{5-\sqrt{5}}{20} \text{ and } s = \frac{5+3\sqrt{5}}{20}$$

Fourth order (centroid and four interior points):

Point location	Weight
$(\frac{1}{4}, \frac{1}{4}, \frac{1}{4}, \frac{1}{4})$	$-\frac{4}{5}$
$(\frac{1}{6}, \frac{1}{6}, \frac{1}{6}, \frac{1}{2})$	$\frac{9}{20}$
$(\frac{1}{6}, \frac{1}{6}, \frac{1}{2}, \frac{1}{6})$	$\frac{9}{20}$
$(\frac{1}{6}, \frac{1}{2}, \frac{1}{6}, \frac{1}{6})$	$\frac{9}{20}$
$(\frac{1}{2}, \frac{1}{6}, \frac{1}{6}, \frac{1}{6})$	$\frac{9}{20}$

Just as in the two-dimensional case, this last quadrature rule includes a negative weight for the centroid, which may be problematical in practice.

IV. Curved Boundaries

Perhaps the most challenging aspect of achieving high-order accuracy is correct treatment of curved boundaries. There are four distinct components to curved boundary treatment: flux integration along boundaries, flux integration for interior sides of boundary control volumes, computation of control volume moments for boundary control volumes, and integration over control volumes with curved boundaries, both for source terms and for computing exact control volume averages for comparison when validating a code. In all of these cases, the key issue is that the curved boundary and its piecewise linear representation (as line segments between boundary vertices) are separated by a distance that is $O(h^2)$ for edge length h . In general, the discrete approximation of the boundary must approach the true underlying boundary shape with the same order of accuracy as the discretization scheme.

A. Flux Integration Along Curved Boundaries

When integrating fluxes along curved boundaries, care must be taken that the solution values, boundary normals, and integration weights accurately reflect the shape of the boundary. Perhaps the most straightforward way to do this is to use the boundary representation directly in setting up Gauss integration points. In two dimensions, Gauss point locations are determined as fractions of arc length. Normals at Gauss points are found by querying the boundary representation directly. Finally, Gauss weights are assigned based on arc length (2D) or on surface area (3D).

To illustrate the differences between exact and inexact approximations to Gauss point location, let us consider three possible choices in two dimensions, for a circular arc with radius of curvature R , shown in Figure 6.^c The coordinate system is centered at the center of curvature of the arc, with x pointing the right and y pointing up. The three choices of Gauss point considered are:

^cThis choice of geometry is not as restrictive as it sounds, in that any well-resolved curve (where $l \ll R$) asymptotically resembles a circular arc.

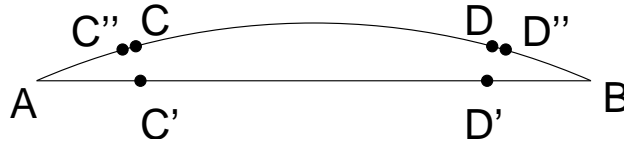


Figure 6. Curved boundary arc AB and its approximation by a straight line segment. The radius of curvature of the arc is R . The coordinate system is centered at the center of curvature of the arc, with x pointing the right and y pointing up.

1. The correct Gauss point locations, based on distance along the arc \widehat{AB} ; these are labeled C and D in the figure.
2. The “correct” Gauss point locations for the segment \overrightarrow{AB} , labeled C' and D' .
3. The normal projections of points C' and D' onto the arc, labeled C'' and D'' .

	D	D'	D''
x	$R \sin \frac{\theta}{\sqrt{3}}$	$R \frac{\sin \theta}{\sqrt{3}}$	$R \frac{\sin \theta}{\sqrt{2 \cos^2 \theta + 1}}$
y	$R \cos \frac{\theta}{\sqrt{3}}$	$R \cos \theta$	$R \cos \theta \sqrt{\frac{3}{2 \cos^2 \theta + 1}}$
Weight	$R\theta$	$\frac{l}{2}$	$R\theta$
Normal Direction	$\frac{\pi}{2} - \frac{\theta}{\sqrt{3}}$	$\frac{\pi}{2}$	$\frac{\pi}{2} - \arctan \frac{\sin \theta}{\sqrt{3} \cos \theta}$
x -location Error	—	$\frac{\sqrt{3}}{216} \frac{l^3}{R^2}$	$-\frac{\sqrt{3}}{108} \frac{l^3}{R^2}$
y -location Error	—	$\frac{l^2}{12R}$	$\frac{l^4}{216R^3}$
Weight Error	—	$\frac{l^3}{48R^2}$	0
Normal Angle Error	—	$\frac{\theta}{\sqrt{3}}$	$\frac{2\sqrt{3}}{27} \theta^3$

Table 3. Comparison of Gauss integration data for the correct and two incorrect methods for finding Gauss points.

Finding the locations, weights, and normals for these points is a straightforward exercise in trigonometry; the results are given in Table 3 for points D , D' , and D'' ; only leading-order error terms are retained. As expected, the straight line segment is a poor approximation, yielding a second-order error in the y -component of Gauss point location; this error implies a second-order error in the value of the reconstruction polynomial R_i that will be computed at the Gauss points. The normal direction is only first-order in θ and therefore in l (which can be written as $l = 2R \sin \theta$); note that this implies only a second-order difference in the end locations of the normal vectors and therefore of the dot product computed as part of the flux integration. Taking the segment Gauss point C' and projecting it normally onto the arc makes the dominant error a third-order error in the x -component of the Gauss point location. Assuming that the Gauss weights are computed as half the true arc length, using C'' is therefore a third-order accurate choice, in general.

To demonstrate the effect of proper versus improper handling of curved boundaries, we consider the case of an inviscid supersonic vortex, as described in Aftosmis and Berger.²³ We choose an inner radius of 2, an outer radius of 3, and an inlet Mach number at the inner boundary of 2. With proper boundary treatment, the solution error has the same asymptotic behavior as the reconstruction, converging at the nominal order of accuracy, as seen in Figure 7 for cell-centered control volumes. Failing to account for boundary curvature in flux integration, however, leads to disappointing results. Figure 8 shows the effect of treating curved boundary edges as straight line segments instead of genuinely curved; this is the only difference between the solutions in the two parts of that figure. The errors are much larger when incorrect quadrature data is used, and these errors occur exclusively at and near curved boundaries.^d

B. Control Volume Moments along Curved Boundaries

Control volume moments for control volumes adjacent to curved boundaries must also be computed with care. Because we compute moments by applying Gauss’s theorem to convert integration over the control volume to integration

^dThese pictures report the data that the text describes, but for a circular advection-diffusion problem instead of the supersonic vortex. The final paper will of course include error plots based on the supersonic vortex problem. We will also consider the use of points C'' and D'' as quadrature points; the analysis implies that this choice will be adequate for third-order accuracy.

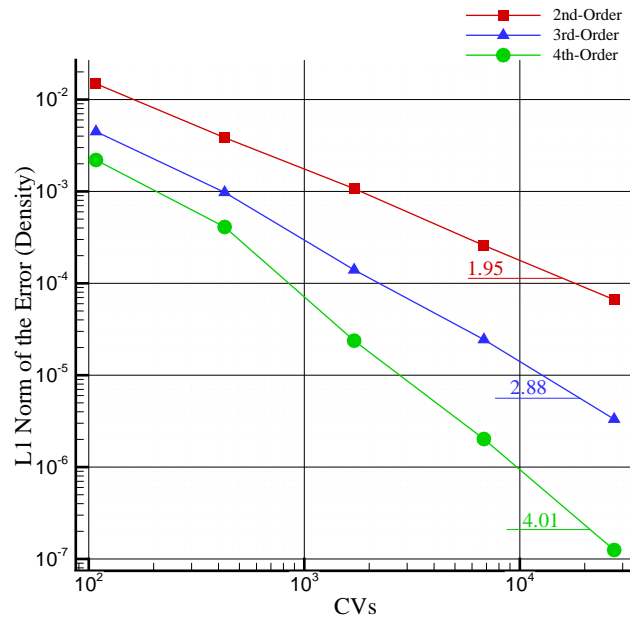
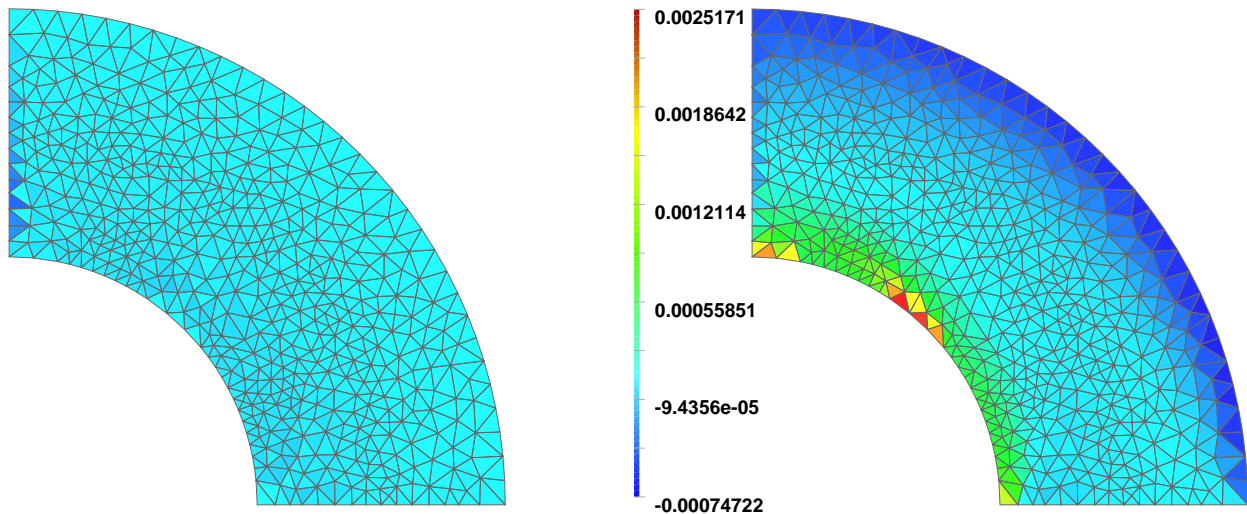


Figure 7. When curved boundaries are properly accounted for, the solution error converges at the same asymptotic rate as the reconstruction error.



(a) Fourth-order schemed with correct Gauss data (points C and D of Figure 6).

(b) Fourth-order schemed with Gauss points on a straight line segment instead of the curved control volume boundary (points C' and D' of Figure 6).

Figure 8. Using the wrong quadrature data for a curved boundary has a serious effect on accuracy. This figure shows the solution error for a fourth-order, cell-centered scheme with and without proper flux quadrature at the boundary. Both plots show error with the same scale.

around the control volume, our concern here is with accurate placement of Gauss integration points along the curved boundaries, based on arclength. Because of the curvature of the boundary, the Cartesian coordinates x and y are non-linear functions of the boundary arc length s . This implies that high-order integration along the boundary is always required. As a result, we choose to use three-point quadrature for all curved boundary segments, making the quadrature sixth-order accurate, which is more than enough to ensure that we can always compute terms at least as complex as the highest-order moments sufficiently accurately.

[The final version of the paper will show the differences between supersonic vortex calculations with differing degrees of accuracy in the boundary moment calculations.]

C. Integration over the Interior of Control Volumes along Curved Boundaries

The final key point in accurately handling control volumes with curved boundaries is integration over the interior of these control volumes. For control volumes which have straight sides, we use Gauss integration over triangles or tetrahedra, as described in Section III. For control volumes with curved sides, we could extend that approach using ideas from isoparametric finite elements, but we choose instead to formulate an integration scheme that eliminates the need for decomposition of vertex-centered control volumes into triangles/tetrahedra. Our approach chooses integration points and weights to ensure that polynomials of degree $\leq k - 1$ are integrated exactly, which in turn guarantees that the integration is k^{th} -order accurate. Mathematically, this requires that, for any monomial of degree $\leq k - 1$,

$$\sum_i w_i x_i^m y_i^n = \frac{1}{A} \int_{\text{CV}} x^m y^n dA$$

and similarly in three dimensions; note that this requirement can be restated in words by saying that the weighted moments of the integration points must match the moments of the region being integrated, up to moments of the order $k - 1$. In principle we could use a very small number of integration points — potentially as few as two for a third-order 2D scheme, for instance, or as few as five for a fourth-order 3D scheme — as there are $d + 1$ degrees of freedom per integration point in d dimensions. However, we have found that the resulting non-linear systems of equations are intractable analytically. Instead, our approach has been to select enough integration points that we can specify \vec{x}_i and solve for w_i . The expressions involved are lengthy, and are given in Appendix A. By design, these integration schemes are exact for low degree monomials, and therefore are k^{th} order accurate when implemented to match the $k - 1$ degree moments.

[In the final version of the paper, we will include figures comparing the control volume averages of the exact supersonic vortex solution to the computed solutions with the correct and various simplified techniques for control volume integration.]

V. Conclusions

This paper describes in detail a number of sometimes obscure aspects of correctly implementing a high-order accurate unstructured mesh finite-volume solver. We discuss reconstruction, flux integration, curved boundary treatment, and demonstrating order of accuracy. In each case, we describe test cases appropriate for confirming correct behavior of a high-order code, as well as demonstrating some of the common pitfalls in implementation and showing their effects. We hope that this paper will serve other researchers as a practical guide to creating their own high-order accurate solvers.

Acknowledgments

This work was supported by the Canadian Natural Sciences and Engineering Research Council under Grant OPG-0194467.

References

- ¹Barth, T. J. and Frederickson, P. O., “Higher Order Solution of the Euler Equations on Unstructured Grids Using Quadratic Reconstruction,” AIAA paper 90-0013, Jan. 1990.
- ²Barth, T. J., “Recent Developments in High Order K-Exact Reconstruction on Unstructured Meshes,” AIAA paper 93-0668, Jan. 1993.
- ³Abgrall, R., “On Essentially Non-oscillatory Schemes on Unstructured Meshes: Analysis and Implementation,” *Journal of Computational Physics*, Vol. 114, No. 1, 1994, pp. 45–58.
- ⁴Ollivier-Gooch, C. F., “High-Order ENO Schemes for Unstructured Meshes Based on Least-Squares Reconstruction,” AIAA paper 97-0540, Jan. 1997.
- ⁵Delanaye, M. and Essers, J. A., “Quadratic-reconstruction finite volume scheme for compressible flows on unstructured adaptive grids,” *American Institute of Aeronautics and Astronautics Journal*, Vol. 35, No. 4, April 1997, pp. 631–639.
- ⁶Geuzaine, P., Delanaye, M., and Essers, J.-A., “Computation of High Reynolds Number Flows with an Implicit Quadratic Reconstruction Scheme on Unstructured Grids,” *Proceedings of the Thirteenth AIAA Computational Fluid Dynamics Conference*, American Institute of Aeronautics and Astronautics, 1997, pp. 610–619.

- ⁷Friedrich, O., “Weighted Essentially Non-Oscillatory Schemes for the Interpolation of Mean Values on Unstructured Grids,” *Journal of Computational Physics*, Vol. 144, No. 1, July 1998, pp. 194–212.
- ⁸Hu, C. Q. and Shu, C. W., “Weighted essentially non-oscillatory schemes on triangular meshes,” *Journal of Computational Physics*, Vol. 150, No. 1, March 1999, pp. 97–127.
- ⁹Agarwal, R. K. and Halt, D. W., “A compact high-order unstructured grids method for the solution of Euler equations,” *International Journal for Numerical Methods in Fluids*, Vol. 31, No. 1, Sept. 1999, pp. 121–147.
- ¹⁰Rogers, S. E., Kwak, D., and Kiris, C., “Steady and Unsteady Solutions of the incompressible Navier-Stokes Equations,” *American Institute of Aeronautics and Astronautics Journal*, Vol. 29, No. 4, April 1991, pp. 603–610.
- ¹¹Zingg, D., De Rango, S., Nemec, M., and Pulliam, T., “Comparison of Several Spatial Discretizations for the Navier-Stokes Equations,” *Journal of Computational Physics*, Vol. 160, 2000, pp. 683–704.
- ¹²De Rango, S. and Zingg, D. W., “Higher-order spatial discretization for turbulent aerodynamic computations,” *American Institute of Aeronautics and Astronautics Journal*, Vol. 39, No. 7, July 2001, pp. 1296–1304.
- ¹³Ollivier-Gooch, C. F., “Quasi-ENO Schemes for Unstructured Meshes Based on Unlimited Data-Dependent Least-Squares Reconstruction,” *Journal of Computational Physics*, Vol. 133, No. 1, 1997, pp. 6–17.
- ¹⁴Ollivier-Gooch, C. F. and Van Altena, M., “A High-order Accurate Unstructured Mesh Finite-Volume Scheme for the Advection-Diffusion Equation,” *Journal of Computational Physics*, Vol. 181, No. 2, 2002, pp. 729–752.
- ¹⁵Nejat, A. and Ollivier-Gooch, C., “A High-Order Accurate Unstructured GMRES Solver for the Euler Equations,” Presented at the Third International Conference on CFD, June 2004.
- ¹⁶Michalak, K. and Ollivier-Gooch, C., “Parallelization of a High-Order-Accurate Unstructured Mesh Finite-Volume Solver,” *Proceedings of the Twelfth Annual Conference of the Computational Fluid Dynamics Society of Canada, Société canadienne de CFD / CFD Society of Canada*, 2004.
- ¹⁷Nejat, A. and Ollivier-Gooch, C., “A High-Order Accurate Unstructured GMRES Algorithm for Inviscid Compressible Flows,” *Proceedings of the Seventeenth AIAA Computational Fluid Dynamics Conference*, American Institute of Aeronautics and Astronautics, June 2005.
- ¹⁸Ollivier-Gooch, C., “On k -exact Integration over Arbitrary Polygons and Polyhedra,” *Applied Mathematics and Computation*, Vol. In preparation, 2006.
- ¹⁹Mavriplis, D. J., “Revisiting the least-squares procedure for gradient reconstruction on unstructured meshes,” *Proceedings of the 16th AIAA Computational Fluid Dynamics Conference*, 2003.
- ²⁰Anderson, W. K. and Bonhaus, D. L., “An Implicit Upwind Algorithm for Computing Turbulent Flows on Unstructured Grids,” *Computers and Fluids*, Vol. 23, No. 1, Jan. 1994, pp. 1–21.
- ²¹Stroud, A. H. and Secrest, D., *Gaussian Quadrature Formulas*, Prentice-Hall, Englewood Cliffs, N.J., 1966.
- ²²Roache, P. J., “Code Verification by the Method of Manufactured Solutions,” *Journal of Fluids Engineering*, Vol. 124, No. 1, March 2002, pp. 4–10.
- ²³Aftosmis, M. J. and Berger, M. J., “Multilevel Error Estimation and Adaptive h -refinement for Cartesian Meshes with Embedded Boundaries,” AIAA paper 2002-0863., Jan. 2002.

A. Integration Over Irregularly-Shaped Control Volumes, Including Those With Curved Boundaries

In two dimensions, we seek to match the low-degree moments of the control volume so that we can exactly integrate low-degree polynomials. This requires that the integration points and weights satisfy

$$\sum_i w_i x_i^m y_i^n z_i^p = \frac{1}{V} \int_{\text{CV}} x^m y^n z^p dV$$

We will not derive the results here, referring interested readers instead to.¹⁸ All the integration rules are expressed in a coordinate frame shifted to have its origin at the reference point of the control volume, and with normalized weights.

A. Two Dimensions

1. Second Order

In this case, a single point at the control volume centroid suffices, with a weight of 1.

2. Third Order

In this case, six points are used, four at the corners of a square centered at the control volume reference point, and one on each of the positive coordinate axes where the axes cross the square. First, we define

$$r \equiv \sqrt{x^2 + y^2}$$

Then we can write the integration data as:

x_i	y_i	w_i
r	r	$-\frac{3}{4} + \frac{\bar{x}}{4r} + \frac{\bar{y}}{4r} + \frac{\bar{x}^2}{2r^2} + \frac{\bar{xy}}{4r^2} + \frac{\bar{y}^2}{2r^2}$
$-r$	r	$-\frac{1}{4} + \frac{\bar{x}}{4r} + \frac{\bar{y}}{4r} + \frac{\bar{x}^2}{2r^2} - \frac{\bar{xy}}{4r^2}$
$-r$	$-r$	$\frac{1}{4} - \frac{\bar{x}}{4r} - \frac{\bar{y}}{4r} + \frac{\bar{xy}}{4r^2}$
r	$-r$	$-\frac{1}{4} + \frac{\bar{x}}{4r} - \frac{\bar{y}}{4r} - \frac{\bar{xy}}{4r^2} + \frac{\bar{y}^2}{2r^2}$
r	0	$1 - \frac{\bar{y}^2}{r^2}$
0	r	$1 - \frac{\bar{x}^2}{r^2}$

3. Fourth Order

In this, the ten required points are distributed on two concentric circles. Each circle has five equidistributed points; one circle has a point on the positive x -axis, the other on the negative x -axis. First, define normalized control volume moments, using a length scale related to the radius of gyration of the control volume:

$$\begin{aligned}
 h &\equiv \sqrt{\frac{\overline{x^2 + y^2}}{12}} \\
 \bar{u} &\equiv \frac{\bar{x}}{h} \\
 \bar{v} &\equiv \frac{\bar{y}}{h} \\
 \overline{u^2} &\equiv \frac{\overline{x^2}}{h^2} \\
 \overline{uv} &\equiv \frac{\overline{xy}}{h^2} \\
 \overline{v^2} &\equiv \frac{\overline{y^2}}{h^2} \\
 \overline{u^3} &\equiv \frac{\overline{x^3}}{h^3} \\
 \overline{u^2y} &\equiv \frac{\overline{x^2y}}{h^3} \\
 \overline{uv^2} &\equiv \frac{\overline{xy^2}}{h^3} \\
 \overline{v^3} &\equiv \frac{\overline{y^3}}{h^3}
 \end{aligned}$$

Then the radii of the two circles on which integration points are located are

$$\begin{aligned}
 r_1 &= \frac{h\sqrt{6}}{8} \\
 r_2 &= \frac{h\sqrt{6}\sqrt{7}}{24}
 \end{aligned}$$

This choice of radii ensures that each circle of points has exactly half of the total integration weight. The locations of the integration points are given by:

i	x_i	y_i
1	r_1	0
2	$r_1 \cos \frac{2\pi}{5}$	$r_1 \sin \frac{2\pi}{5}$
3	$r_1 \cos \frac{4\pi}{5}$	$r_1 \sin \frac{4\pi}{5}$
4	$r_1 \cos \frac{4\pi}{5}$	$-r_1 \sin \frac{4\pi}{5}$
5	$r_1 \cos \frac{2\pi}{5}$	$-r_1 \sin \frac{2\pi}{5}$
6	$-r_2$	0
7	$-r_2 \cos \frac{2\pi}{5}$	$r_2 \sin \frac{2\pi}{5}$
8	$-r_2 \cos \frac{4\pi}{5}$	$r_2 \sin \frac{4\pi}{5}$
9	$-r_2 \cos \frac{4\pi}{5}$	$-r_2 \sin \frac{4\pi}{5}$
10	$-r_2 \cos \frac{2\pi}{5}$	$-r_2 \sin \frac{2\pi}{5}$

The weights are:

$$\begin{aligned}
w_1 &= -\frac{7}{10} - 4 \cdot \frac{7\sqrt{6}}{15} \bar{u} + 2 \cdot \frac{8T_6}{15} \left((86 + 33\sqrt{7}) \bar{u}^2 + (58 + 21\sqrt{7}) \bar{v}^2 + 8T_{14} \sqrt{6u^3} + 24T_{16} \sqrt{6uv^2} \right) \\
w_2 &= -\frac{7}{10} - \frac{7}{15} \left(\sqrt{6} (\sqrt{5} - 1) \bar{u} + 2T_5 \bar{v} \right) + \frac{8T_6}{15} \left(-(-T_2 + T_1) \bar{u}^2 + T_9 (-T_4 + T_1) \bar{u}\bar{v} + (T_3 + T_1) \bar{v}^2 \right) \\
&\quad + \frac{8T_6}{15} \left(4(T_{11} - T_{14}) \sqrt{6u^3} - 12T_5 (T_{12} - T_{15}) \bar{u}^2 \bar{v} + 12(T_{13} - T_{16}) \sqrt{6uv^2} + 4T_5 (T_{12} + T_{17}) \bar{v}^3 \right) \\
w_3 &= -\frac{7}{10} + \frac{7}{15} \left(\sqrt{6} (\sqrt{5} + 1) \bar{u} - 2T_7 \bar{v} \right) + \frac{8T_6}{15} \left((T_2 + T_1) \bar{u}^2 - T_{10} (T_4 + T_1) \bar{u}\bar{v} - (-T_3 + T_1) \bar{v}^2 \right) \\
&\quad + \frac{8T_6}{15} \left(-4(T_{11} + T_{14}) \sqrt{6u^3} + 12T_7 (T_{12} + T_{15}) \bar{u}^2 \bar{v} - 12(T_{13} + T_{16}) \sqrt{6uv^2} - 4T_7 (T_{12} - T_{17}) \bar{v}^3 \right) \\
w_4 &= -\frac{7}{10} + \frac{7}{15} \left(\sqrt{6} (\sqrt{5} + 1) \bar{u} + 2T_7 \bar{v} \right) + \frac{8T_6}{15} \left((T_2 + T_1) \bar{u}^2 + T_{10} (T_4 + T_1) \bar{u}\bar{v} - (-T_3 + T_1) \bar{v}^2 \right) \\
&\quad + \frac{8T_6}{15} \left(-4(T_{11} + T_{14}) \sqrt{6u^3} - 12T_7 (T_{12} + T_{15}) \bar{u}^2 \bar{v} - 12(T_{13} + T_{16}) \sqrt{6uv^2} + 4T_7 (T_{12} - T_{17}) \bar{v}^3 \right) \\
w_5 &= -\frac{7}{10} - \frac{7}{15} \left(\sqrt{6} (\sqrt{5} - 1) \bar{u} - 2T_5 \bar{v} \right) + \frac{8T_6}{15} \left(-(-T_2 + T_1) \bar{u}^2 - T_9 (-T_4 + T_1) \bar{u}\bar{v} + (T_3 + T_1) \bar{v}^2 \right) \\
&\quad + \frac{8T_6}{15} \left(4(T_{11} - T_{14}) \sqrt{6u^3} + 12T_5 (T_{12} - T_{15}) \bar{u}^2 \bar{v} + 12(T_{13} - T_{16}) \sqrt{6uv^2} - 4T_5 (T_{12} + T_{17}) \bar{v}^3 \right) \\
w_6 &= \frac{9}{10} - 4 \cdot \frac{9T_6}{35} \sqrt{6} T_{21} \bar{u} + 2 \cdot \frac{24T_6}{35} \left(-(38 + 15\sqrt{7}) \bar{u}^2 - (27\sqrt{7} + 74) \bar{v}^2 + 8T_{30} \sqrt{6u^3} + 8T_{23} \sqrt{6uv^2} \right) \\
w_7 &= \frac{9}{10} - \frac{9T_6}{35} \left(-(T_{11} - T_{21}) \sqrt{6} \bar{u} + 2T_5 T_{21} \bar{v} \right) + \frac{24T_6}{35} \left((3T_{12} - T_{25}) \bar{u}^2 - 3T_9 (T_{12} - T_{26}) \bar{u}\bar{v} + (3T_{12} - T_{24}) \bar{v}^2 \right) \\
&\quad + \frac{24T_6}{35} \left(4(T_{29} - T_{30}) \sqrt{6u^3} - 4T_5 (3T_{12} + T_{22}) \bar{u}^2 \bar{v} + 4(-T_{23} + T_{27}) \sqrt{6uv^2} + 4T_5 (T_{12} - T_{17}) \bar{v}^3 \right) \\
w_8 &= \frac{9}{10} + \frac{9T_6}{35} \left((T_{11} + T_{21}) \sqrt{6} \bar{u} + 2T_7 T_{21} \bar{v} \right) + \frac{24T_6}{35} \left((3T_{12} - T_{25}) \bar{u}^2 + 3T_{10} (T_{12} + T_{26}) \bar{u}\bar{v} - (3T_{12} + T_{24}) \bar{v}^2 \right) \\
&\quad + \frac{24T_6}{35} \left(-4(T_{29} + T_{30}) \sqrt{6u^3} + 4T_7 (3T_{12} - T_{22}) \bar{u}^2 \bar{v} - 4(T_{23} + T_{27}) \sqrt{6uv^2} - 4T_7 (T_{12} + T_{17}) \bar{v}^3 \right) \\
w_9 &= \frac{9}{10} + \frac{9T_6}{35} \left((T_{11} + T_{21}) \sqrt{6} \bar{u} - 2T_7 T_{21} \bar{v} \right) + \frac{24T_6}{35} \left((3T_{12} - T_{25}) \bar{u}^2 - 3T_{10} (T_{12} + T_{26}) \bar{u}\bar{v} - (3T_{12} + T_{24}) \bar{v}^2 \right) \\
&\quad + \frac{24T_6}{35} \left(-4(T_{29} + T_{30}) \sqrt{6u^3} - 4T_7 (3T_{12} - T_{22}) \bar{u}^2 \bar{v} - 4(T_{23} + T_{27}) \sqrt{6uv^2} + 4T_7 (T_{12} + T_{17}) \bar{v}^3 \right) \\
w_{10} &= \frac{9}{10} + \frac{9T_6}{35} \left(-(T_{11} - T_{21}) \sqrt{6} \bar{u} - 2T_5 T_{21} \bar{v} \right) + \frac{24T_6}{35} \left(-(3T_{12} + T_{25}) \bar{u}^2 + 3T_9 (T_{12} - T_{26}) \bar{u}\bar{v} + (3T_{12} - T_{24}) \bar{v}^2 \right) \\
&\quad + \frac{24T_6}{35} \left(4(T_{29} - T_{30}) \sqrt{6u^3} + 4T_5 (3T_{12} + T_{22}) \bar{u}^2 \bar{v} + 4(-T_{23} + T_{27}) \sqrt{6uv^2} - 4T_5 (T_{12} - T_{17}) \bar{v}^3 \right)
\end{aligned}$$

Finally, we must define all of the temporary variables used in the weights, some of which are defined in

terms of still other variables:

$$T_1 = 7\sqrt{5} + 3\sqrt{35}$$

$$T_2 = 137 + 51\sqrt{7}$$

$$T_3 = 151 + 57\sqrt{7}$$

$$T_4 = 7 + 3\sqrt{7}$$

$$T_5 = (\sqrt{5} + 1)\sqrt{3\sqrt{5}}$$

$$T_6 = \frac{1}{3\sqrt{7} + 8}$$

$$T_7 = (\sqrt{5} - 1)\sqrt{3\sqrt{5}}$$

$$T_9 = (\sqrt{5} + 1)\sqrt{2\sqrt{5}}$$

$$T_{10} = (\sqrt{5} - 1)\sqrt{2\sqrt{5}}$$

$$T_{11} = 21\sqrt{5} + 8\sqrt{35}$$

$$T_{12} = 3\sqrt{5} + \sqrt{35}$$

$$T_{13} = 11\sqrt{5} + 4\sqrt{35}$$

$$T_{14} = 27 + 10\sqrt{7}$$

$$T_{15} = 19 + 7\sqrt{7}$$

$$T_{16} = 5 + 2\sqrt{7}$$

$$T_{16} = 45 + 17\sqrt{7}$$

$$T_{21} = 8\sqrt{7} + 21$$

$$T_{22} = 13\sqrt{7} + 33$$

$$T_{23} = 11\sqrt{7} + 30$$

$$T_{24} = 39\sqrt{7} + 103$$

$$T_{25} = 45\sqrt{7} + 121$$

$$T_{26} = \sqrt{7} + 3$$

$$T_{28} = 12\sqrt{5} + 5\sqrt{35}$$

$$T_{29} = 24\sqrt{5} + 8\sqrt{35}$$

$$T_{30} = T_{15} - 1$$